Article:
Ramírez-González, J. and West, A.R. orcid.org/0000-0002-5492-2102 (2020) Electrical properties of calcia-stabilised zirconia ceramics. Journal of the European Ceramic Society, 40 (15). pp. 5602-5611. ISSN 0955-2219

https://doi.org/10.1016/j.jeurceramsoc.2020.06.023

Electrical properties of calcia-stabilised zirconia ceramics

Julia Ramírez-González* and Anthony R. West*

Department of Materials Science and Engineering, The University of Sheffield, Mappin Street, Sheffield S1 3JD, UK

Abstract

The electrical properties of cubic, calcia-stabilised zirconia ceramics, $Ca_xZr_{1-x}O_{2-x}$: $0.12 \leq x \leq 0.18$ have been investigated using impedance spectroscopy to separate bulk, grain boundary and electrode contact impedances. ~~In order to characterise accurately the bulk response, it was found~~ The most appropriate equivalent circuit to characterise the bulk response required inclusion of a dielectric component, represented by a series RC element, in parallel with the oxide ion conductivity represented by a parallel combination of a resistance, capacitance and constant phase element. The dielectric component may be attributed to defect complexes involving immobile oxygen vacancy pairs whereas long range conduction involves single oxygen vacancies.

Keywords: Calcia-stabilised zirconia; impedance spectroscopy; dipole relaxation; oxide ion conduction; defect complexes

1. Introduction

Zirconia-based materials with defect fluorite structures are widely used as solid electrolytes for fuel cell and sensor applications [1]–[4]. To optimise properties, compositional control includes the addition of dopants that stabilise the cubic polymorph: Y is the main dopant for fuel cell electrolytes in yttria-stabilised zirconia, YSZ, but Sc is of interest because of the higher conductivity of Sc-doped materials [5]. The technology of these materials as solid electrolytes is well-developed but numerous scientific issues remain to be clarified which may lead to property improvements.

First, impedance analysis of YSZ ceramics generally shows the common presence of grain boundary impedances in addition to bulk impedances [6], but their origin is not well-understood and they are not readily eliminated by attention to ceramic processing procedures. Second, the commonly-observed curvature of conductivity Arrhenius plots at high temperatures is not well-explained [7]–[13]. Early viewpoints attributed it to a transition from trapped to free oxide ion vacancies, but the reality is now thought to be considerably more complex, especially since the high yttria content of high conductivity materials makes it difficult to envisage how oxygen vacancies can be well-separated from the Y dopant. Third, recent studies on YSZ ceramics and single crystals show that dielectric or dipolar elements contribute to the overall bulk impedance and must be considered in full analysis of impedance data [14]. Fourth, whilst solid electrolyte applications require the absence of any electronic conduction, *p*-type conductivity can be induced in YSZ on application of a small *dc* bias [15] and in yttria-rich YSZ compositions, by simply making impedance measurements in oxygen [16].

We are interested in calcia-stabilised zirconia, $Ca_xZr_{1-x}O_{2-x}$, CSZ, as a model system to investigate some of the above issues and also, as a prelude to using impedance spectroscopy, IS, to study the early stages of flash sintering phenomena, which were discovered using YSZ materials [17] . ~~has been studied widely for its high level of oxide ion conductivity leading to possible sensor and fuel cell applications~~. Early literature, pre-1970, on CSZ, including the stoichiometry range of cubic solid solutions at different temperatures and their electrical properties is fully covered in [18] ~~and only key points from~~

*Corresponding authors.
E-mail address: jramirezgonzalez1@sheffield.ac.uk, a.r.west@sheffield.ac.uk

~~it are highlighted here~~. Other fluorite-structured solid oxide electrolytes based on ZrO_2, ThO_2, CeO_2 and HfO_2 are also reviewed in [18]. The cubic polymorph of pure zirconia is thermodynamically stable only at very high temperatures, but phase equilibrium studies show that it is stabilised to lower temperatures by numerous aliovalent substituents such as Ca^{2+}, Mg^{2+} and Y^{3+}, in which charge compensation is achieved by oxygen vacancy creation. The advantages of such cubic stabilised materials ~~for high temperature applications~~ are that, not only are they very good oxide ion conductors because of the high concentration of oxygen vacancies, but also the disruptive cubic-tetragonal-monoclinic phase changes that are observed on cooling undoped ZrO_2 [19], [20] are not observed ~~in the cubic-stabilised materials~~.

The most recent CaO-ZrO_2 phase diagram [20], shows an extensive range of cubic solid solutions, $0.14<x<0.18$ at 1300 ^oC which increases to $0.06<x<0.21$ at 2000 ^oC. According to the phase diagram, the cubic solid solutions should decompose below a eutectoid temperature of 1066 ^oC, but the transformation rate is very slow and cubic, single phase materials may be preserved readily, in a metastable state, to lower temperatures. Several papers, summarised in [18], reported development of a superstructure on annealing samples for long times at ~1000 ^0C. This was attributed to vacancy ordering which occurred more readily with increasing Ca content and was not associated with eutectoid decomposition.

CSZ is an oxide ion conductor over the oxygen partial pressure, pO_2 range $1–10^{-22}$ atm [21]; transport measurements show that conduction is entirely anionic, with cation diffusion coefficients that are 5 orders of magnitude less than oxygen diffusion coefficients [18]. Almost all studies on CSZ and other fluorite-structured solid solution materials assume implicitly that oxygen vacancy creation is the principal charge compensation mechanism on doping with lower-valent cations. However, Diness and Roy, in a little-cited paper [22], showed clear evidence from density measurements of a change from oxygen vacancy compensation to interstitial calcium compensation on heating CSZ samples from 1600 to 1800 ^oC. The possible consequences of such a change in defect structure on electrical properties are not known, although it is noted that an early study of the effect of sintering temperature on ceramic microstructure and electrical properties indicated a possible decrease in total conductivity on heating at 2000 ^oC compared with heating at 1600 ^oC.

The onset of *n*-type conduction that occurs at very low pO_2 has been detected by emf measurements and can be promoted by the addition of donor dopants [23]. The possibility of *p*-type conduction at high pO_2 is envisaged, but was expected to be observed only at extremely high oxygen pressures [24] and has not been observed experimentally. In the absence of Ca doping, however, ZrO_2 does show *p*-type behaviour at high pO_2 [25], [26]

The ~~details of the~~ oxide ion conductivity of ~~CSZ and other~~ fluorite-based oxide ion conductors has received much attention, partly because (i) conductivities pass through a maximum at intermediate oxygen vacancy concentrations and (ii) conductivity Arrhenius plots frequently show a departure from linearity at high temperatures [7]–[10]. A defect-dopant associate model was initially proposed to account for the conductivity maxima [10], [11] and the high temperature curvature widely attributed to the dissociation of defect complexes, thereby allowing values for the defect association and vacancy migration enthalpies to be determined [9]. More recently, however, the validity of the defect dissociation model has been questioned.

Various studies, including neutron and X-ray diffraction and diffuse scattering, neutron quasi-elastic scattering and high temperature neutron diffraction, together with DFT modelling, have led to the suggestion that oxygen vacancies, whether single, paired or aggregated into larger clusters, are key species that influence the composition- and temperature-dependent conductivities of YSZ and scandia-doped zirconia, ScSZ [27]–[30]. Defect structure and diffuse scattering studies of CSZ single crystals with x=0.04, 0.07, 0.10 and 0.15 showed two types of defect in micro-domains based on either a single

oxygen vacancy or a pair of vacancies separated by a Ca^{2+} ion in a <111> orientation [31], [32]. Molecular dynamic studies of CSZ showed a dynamic spatial distribution of oxygen vacancies that tend to locate near areas with high density of Ca dopant [33].

There is a greater number of reports in the literature on defect structures in YSZ and ScSZ and it appears that the variety of defect structures may be greater than with CSZ. In addition to oxygen vacancy pairs, there is evidence for tetragonally-distorted defect clusters at low x and larger aggregates of vacancy pairs at high x in YSZ and ScSZ [27]–[30]. However, ionic size mismatch between aliovalent dopant and host (Zr) cations leads to localised strain effects which cause a repulsion between dopant and oxygen vacancies. The resulting defect structures may then represent a compromise between repulsive strain effects and electrostatic attraction between oppositely-charged defect species.

Single crystals and ceramics of CSZ with different composition have been characterised using impedance spectroscopy [34]–[36]. Bulk, grain boundary and sample-electrode responses were identified, although fitting of the impedance data to equivalent circuits was not reported. It was suggested ~~in early work on CSZ~~ that at high Ca concentrations, the oxygen vacancies may migrate through a continuous network of V_O-Ca_{Zr} defect complexes, without the need to overcome the association energy for the vacancies to escape from the complexes [10].

~~Vendrell *et al*, proposed an equivalent circuit for single crystal yttria stabilised zirconia, YSZ [14], in which, in order to accurately fit the impedance bulk response, it was found necessary to include a dielectric component that could represent dipoles, in parallel with the circuit element that represented long range ionic conduction. The dipole conduction element was speculated to involve short range oxygen vacancy hopping within the defect complexes. It therefore, would not require an activation energy for defect dissociation in addition to that for vacancy hopping.~~ The main purpose of the present study is to characterise the bulk impedance response of polycrystalline CSZ; this made it necessary to also characterise fully the grain boundary response and the suitability of the Randles circuit [37] to model the sample–electrode response. Further details and discussion of the sample-electrode response, and the application of IS to study the response of CSZ to a *dc* bias, will be reported subsequently.

2. Experimental

Powders with composition $Ca_xZr_{1-x}O_{2-x}$: x= 0.10, 0.12, 0.15, 0.18 and 0.20, were prepared by solid-state reaction of $CaCO_3$ (99%, Fisher) and ZrO_2 (99%, Aldrich), which were dried overnight at 180 ^oC and 1000 ^oC respectively prior to weighing. The mixtures were ground manually with acetone using a pestle and mortar, dried and heated in alumina crucibles at 1150 ^oC overnight to decarbonate $CaCO_3$ and start the reaction. Subsequently, the powders were re-ground, pellets 10 mm in diameter were uniaxially pressed at around 98 MPa and heated for 10 h. Temperatures depended on the composition; 1720 ^oC for x=0.10, 1710 ^oC for x=0.12 and 1600 ^oC for x=0.15, 0.18 and 0.20. Pellet densities were ~86%.

Pellets of each composition were crushed and analysed by X-ray powder diffraction with a STOE STADI P diffractometer (Darmstadt, Germany), Cu $K\alpha_1$ radiation. Data were collected from 2θ = 20 to 80 ^{o} and compared to the diffraction pattern of cubic zirconia (PDF card: 01-070-7361) using the JCPDS database. The cubic lattice parameter was determined by least-squares refinement using STOE WinXPOW version 2.25 and Si powder added as internal standard.

The sintered samples were polished metallographically, thermally-etched at 1300 °C for 30 min and sputter-coated with 10 nm of carbon for microstructural analysis. Scanning electron microscopy (SEM)

images were taken on a field-emission scanning electron microscope (FEI Inspect F50) using an acceleration voltage of 15 kV and energy-dispersion analysis of X-rays (EDX) from Oxford Instruments using 20 kV.

For impedance measurements, Pt paste electrodes were applied to both faces of the pellets and dried at 900 ^{o}C for 2 h. Electroded pellets were attached to the Pt leads of an in-house conductivity jig with the facility to vary the atmosphere flowing over the pellet. Impedance measurements were made between 190 and 900 ^{o}C using a Solartron SI 1260 (measurement accuracy ±0.1%) impedance analyser over the frequency range 10 mHz – 1 MHz with a nominal *ac* voltage of 100 mV. Two sets of corrections were made to the collected data: (i) a geometric factor concerning pellet thickness and sample-electrode contact area and (ii) jig characteristics consisting of the blank, open circuit capacitance, typically 6 pF and the closed circuit resistance of, primarily, the leads, 1-2 Ω. Data analysis and equivalent circuit fitting was performed using ZVIEW software (ZVIEW-Impedance Software version 2.4 Scribner Associates).

3. Results

3.1 Materials characterisation

All samples appeared to be single phase and were indexed on a cubic unit cell, space group Fm3m; a representative diffraction pattern is shown in Fig 1(a), for x = 0.15. The lattice parameter increased linearly with composition, inset Fig 1(a), following Vegard's Law. Therefore, single phase samples belonging to the cubic solid solution, $Ca_xZr_{1-x}O_{2-x}$ had been obtained, consistent with the reported homogeneity range at 1600-1700 ^{o}C [20]; these are referred to here as cubic stabilised zirconia, CSZ.

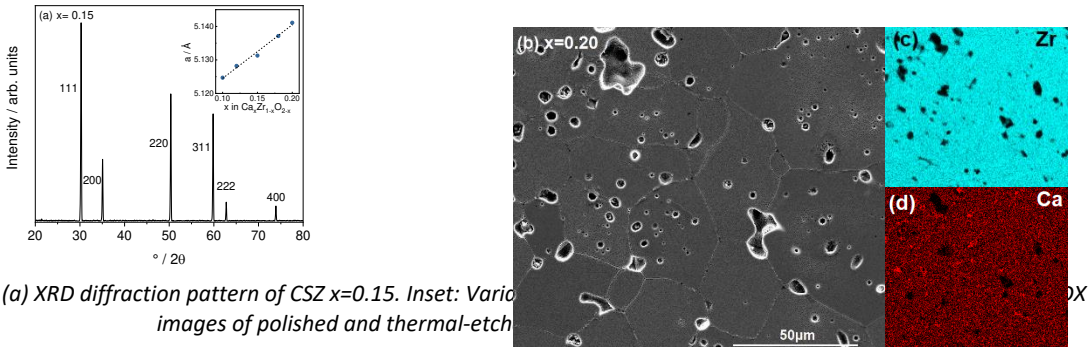

Figure 1*.(a) XRD diffraction pattern of CSZ x=0.15. Inset: Vario* *DX images of polished and thermal-etch*

A typical micro-structure of pellet x=0.20, Figure 1(b), shows grain sizes in the range 10-60 µm and closed porosity, consistent with the measured density of ~86%. No binder or sintering aids were used so as to avoid possible contamination and modification of the impedance results and therefore, no attempt was made to achieve 100% sintered density. Similar microstructures and grain sizes were observed for all compositions. EDX mapping showed a homogeneous distribution of Zr, with evidence of minor traces of Ca segregation around some pores; Hf impurity was detected and presumably originated from the ZrO_2 reagent (~0.30-0.41 At%, according to the Supplier's composition); it was evenly distributed.

3.2 Impedance data

The impedance response of CSZ pellets with composition x = 0.12, 0.15 and 0.18, were measured between 190 and 990 ^{o}C in dry air; similar data sets were obtained for all three compositions. Data for

x = 0.15 at selected temperatures are shown in Fig 2; data for the other two compositions are shown in Supplementary Figs S1 – S2. The impedance complex plane plot for a typical data set at 407 ^{O}C, Fig 2(a), shows two arcs and a large, low frequency curved spike. The same data replotted as a spectroscopic plot of capacitance against frequency in (c) show three regions of almost constant capacitance at low, intermediate and high frequencies. Z''/M'' spectroscopic plots in (d) show a single peak in M'' that overlaps approximately with the high frequency peak in Z'' and is attributed to the bulk response. Finally, the same data replotted as log Y' vs frequency in (e) show plateaux at two intermediate frequencies.

Some additional impedance features are seen at both higher and lower temperatures. First, impedance complex plane plots at higher temperature show that the low frequency curved spike in (a) becomes a broad arc, as shown at 697 ^{o}C in (b), that terminates in a 'tail' extending slightly along the Z' axis at lowest frequencies. Second, the C' data at higher temperatures, eg 936 ^{o}C in (c), show a poorly resolved plateau around 10^{-5}-10^{-4} Fcm^{-1} attributed to the sample-electrode response which becomes a rising dispersion at lowest frequencies. Third, at lower temperatures, eg 199 ^{o}C, (c), the C' data level off at high frequencies to give a clear, frequency-independent plateau around $2x10^{-12}$ Fcm^{-1}, attributable to the frequency-independent, high frequency permittivity, ε' with a value given by $\varepsilon' = C'/e_0$ where e_0 is the permittivity of free space, $8.854x10^{-14}$ Fcm^{-1}.

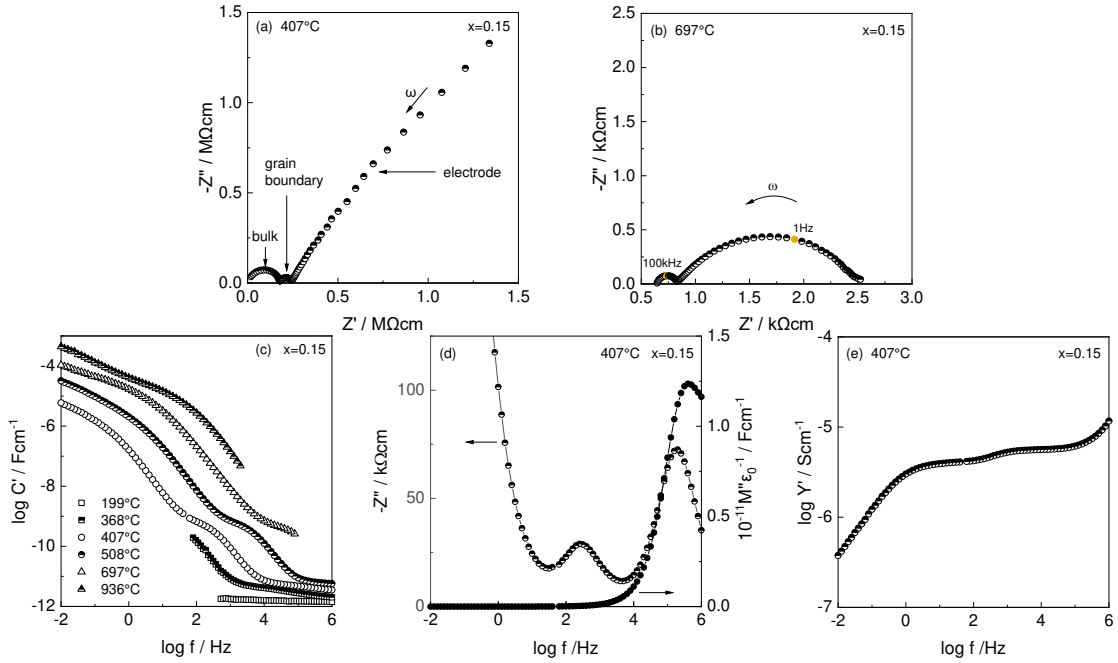

***Figure 2**. (a)-(b) Impedance complex plane plots and spectroscopic plots of (c) capacitance, (d) Z"/M" and (e) admittance spectroscopic plots at different temperatures for x=0.15; ω =2πf.*

Consideration of all these plots and characteristic features together leads to the initial conclusion that the data may be represented by an equivalent circuit that contains three impedance elements connected in series. The arcs shown in (a) and (b) are attributed to, with decreasing frequency, bulk, b, grain boundary, gb and electrode-sample contact, el, impedances. Resistance values were estimated from the intercepts of the arcs on the Z' axis and are shown as conductivity Arrhenius plots in Fig 3(a,b).

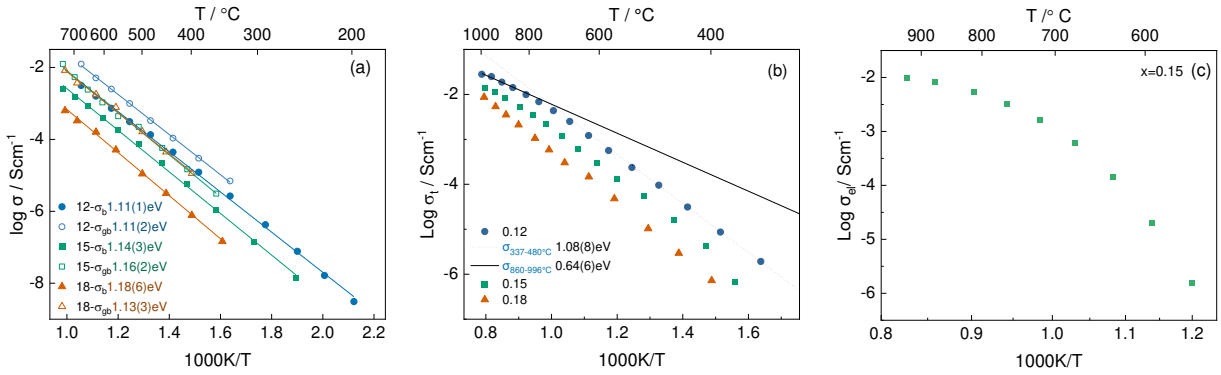

***Figure 3**. Conductivity Arrhenius plots of (a) bulk and grain boundary, (b) total and (c) and electrode resistances.*

In (a), separate plots for grain and grain boundary conductivities are shown at ~200 – 720 °C over which range, both values could be obtained. Activation energy values were estimated assuming linear plots, as shown, although close inspection shows a small amount of curvature in some of the plots. Three general observations may be made. First, all data sets are approximately parallel over this temperature range. Second, both bulk and grain boundary conductivities decrease systematically with increasing Ca content, x. Third, for each composition, although the grain boundary conductivities appear to be higher than the bulk conductivities, the grain boundary values have been corrected only for the overall pellet geometry. The true grain boundary conductivities, after correcting for grain boundary geometry, would be approximately two orders of magnitude smaller and therefore, true grain boundary conductivities are significantly smaller than the bulk conductivities.

At temperatures above 720 °C, only the total sample resistances could be measured and are presented in Fig 3(b) as total conductivities, σ_t. It is clear that these Arrhenius plots show significant curvature at high temperatures, especially for the compositions with highest conductivity. In this sense, the data are similar to those that are well-established for yttria-stabilised zirconia, YSZ, which also show curvature and a systematic decrease in conductivity with higher Y content. Data obtained at high temperatures for the overall conductivity of the sample-electrode impedance, σ_{el}, are shown in (c) and give very non-linear Arrhenius plots with a high activation energy at low temperatures, ≥ 3.0 eV, that levels off to a much smaller value at highest temperatures. Again, the σ_{el} data are corrected only for the overall sample geometry and not for the geometry of the sample-electrode contact**.**

3.3 Equivalent circuits

In order to quantify further the analysis and interpretation of impedance data, the next step is to find the equivalent circuit that gives the best fits to the data and therefore, establish the correct equations to be used to quantify impedance parameters, leading to a description of the behaviour and electrical make-up of the sample. To a first approximation, the impedance data, Fig 2(a,e) indicate an equivalent circuit that contains three impedances, b, gb and el, connected in series. Low temperature data are considered first. These should be, at least partially, free from grain boundary and electrode impedances, thus allowing the bulk response to examined separately and with fewer parameters to be refined. Knowledge of the bulk parameter values and their temperature dependence should also help subsequent fitting to more complex circuits, with more variables, at higher temperatures.

3.3.1 Bulk impedance

A number of equivalent circuits that possibly, could be used to represent the bulk response are shown in Fig 4 and 5, together with the residuals between experimental and fitted impedance data for one

representative composition, x = 0.15 and temperature, 304 ^{0}C in Fig 5; for other compositions and temperatures results are given in Figs S3 and S4. Justification for considering these circuits is as follows. In all cases, the simplest possibility, a resistor, R and capacitor, C in parallel, Fig 4, is considered as the starting point. R would represent the sample resistance and C its capacitance or polarizability. One useful 'thought process' which clarifies why R and C should be placed in parallel is to regard samples as leaky dielectrics; R represents a conduction pathway through the sample that is in parallel with its polarizability.

***Figure 4**. Schematic representation of typical bulk response compared with the ideal response given by a parallel RC element.*

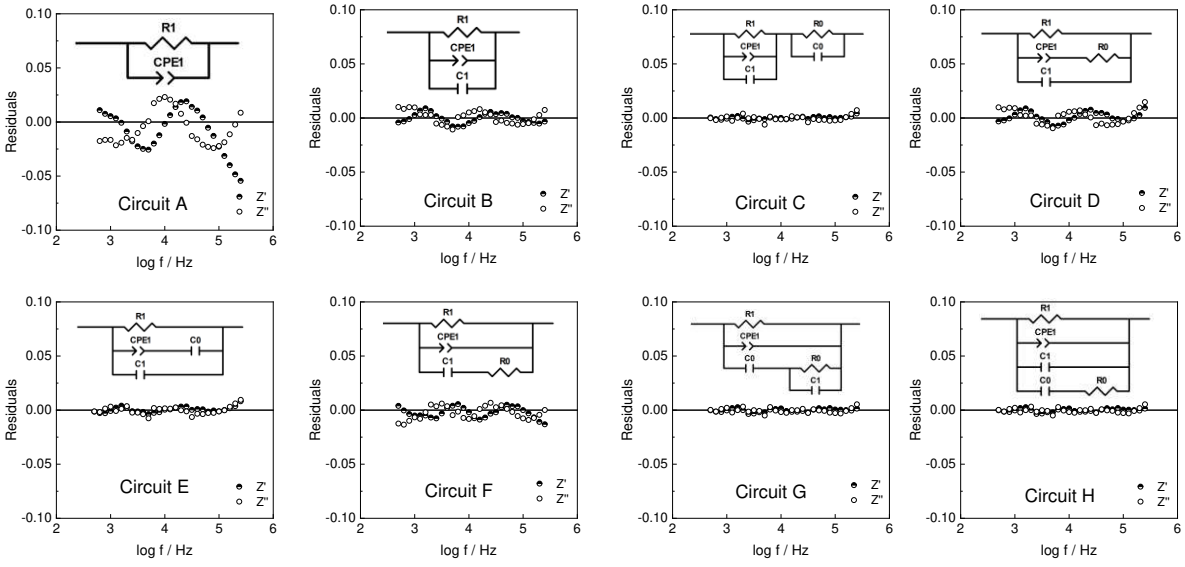

***Figure 5**. Fitting residuals of the bulk response from 8 possible equivalent circuits for x=0.15 at 304°C.*

For the parallel RC element, Fig 4, R and C are single-valued and the parameters Y' and C' are frequency-independent, as shown schematically by the horizontal lines in Fig 4. In practice, Y' and C' are rarely frequency-independent. Instead, Y' data for a bulk response typically show a frequency-independent plateau at lower frequencies which is the *dc* or bulk conductivity plateau, together with an additional high frequency power law dispersion, of slope n when plotted on logarithmic scales, attributed to the ubiquitous Jonscher Law behaviour, Fig 4(a). The onset of a power law response is seen for frequencies > 10^4 Hz in Fig 2(d). As part of the same Jonscher Law behaviour, C' data show a dispersion towards increasing C' values at lower frequencies, below that of the high frequency permittivity plateau, Fig 4(b) and with slope (n-1) on logarithmic scales. This is seen for frequencies over the range 10^4-10^6 Hz in Fig 2(b).

Two circuits are commonly used in the literature to account for non-ideality in equivalent circuits. Both involve inclusion of a constant phase element, CPE, whose admittance is given by $Y^* = A\omega^n + jB\omega^n$. One circuit, A, Fig 5 has a CPE instead of capacitance C. The other, B, has a CPE in addition to, and in parallel with the RC element. Although circuit A is often used to represent impedance data over a limited frequency range [38], [39] and indeed, is included in the widely-used circuit fitting software package [40], it ignores the frequency-independent permittivity shown in many data sets, such as Fig 2(g), particularly at high frequencies and low temperatures. Consequently, fitted values of the CPE parameters obtained using circuit A may be incorrect, especially if the onset of the high frequency capacitance plateau is apparent in the data.

Circuit C, Fig 5, has two impedances connected in series and is the circuit that is used very frequently to represent materials that have both bulk and grain boundary impedances. Depending on the time constants, τ, of the two circuits, given ideally by the magnitude of their RC products, separate arcs may be seen in impedance complex plane plots, as in Fig 2(a) and an intermediate frequency plateau in C' spectroscopic plots, as in Fig 2(c). If the time constants are more similar, then single distorted or asymmetric arcs may be seen in impedance complex plane plots.

Until recently, circuit B has been considered to represent adequately the bulk impedance response of many ionically-conducting materials. However, studies on YSZ ceramics [41] and single crystals [14] showed the need for an additional circuit element to adequately represent the bulk response which was different from addition of a second RC element in series, as in circuit C. The element that was considered most suitable is shown in circuit H and is considered, together with other similar possible circuits, D-G, to model the CSZ data obtained here. All the circuits, D-H, include the possibility of a series-connected RC element in parallel with the bulk conduction element.

This series RC element, considered in isolation, Fig 6, is the element that is regarded to represent dielectric relaxation phenomena, such as dipole reorientation, in materials that show no *dc* conductivity. R_0 represents the resistive component of short range motions involved in the relaxation process; C_0 is viewed as either a blocking capacitance that prevents long range conduction, or as the charge stored by alignment of the dipoles. It is not clear from the literature whether there is a preferred or optimised equivalent circuit to represent such series relaxation processes. Three 'ideal' possibilities are shown in Fig 6; additional possibilities that involve non-ideal behaviour could involve replacement of either capacitance, C_0 or resistance, R_0 by a CPE, but were not found necessary to model the data reported here.

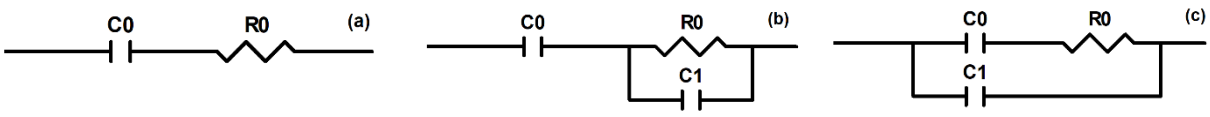

***Figure 6**. Possible equivalent circuits to represent dielectric relaxation phenomena.*

In previous studies of the bulk impedance of YSZ single crystals [14], it was clear that circuit B gave only an approximate fit with rather high residuals between experimental and fitted impedances. Circuit C also did not fit the single crystal data well and anyway, should be inappropriate for a single crystal sample. Circuit H gave a good fit and was justified as being the circuit that represented a combination of the bulk conducting component, circuit B and the simple dielectric element, Fig 6(a). We therefore

made the initial assumption that circuit H may represent the bulk impedance data of the present CSZ ceramics.

Fits to circuit H for all four impedance formalisms are shown for one temperature and composition in Fig 7; impedance residuals are shown for the same data set in Fig 5(h). Fits for other compositions are shown in Fig S5-S6, and fitted parameter values in Tables S1-S3. Excellent agreement between experimental and fitted data is obtained for frequencies above 10^2-10^3 Hz and the residuals are as low as those of any of the other circuits that were tested, and certainly better than those for circuit B. At lowest frequencies, an additional circuit element representing the grain boundary impedance is required to fit the data, especially the C' data, Fig 7, as discussed later. The residuals in Fig 5 show a good fit also for circuit G, which differs from H only in the location of capacitance C_1. The fit for circuit E is slightly less good than for H, but does have one fewer refineable parameter, ie R_1. The fits for circuits A, B, D and F are significantly worse than the other fits.

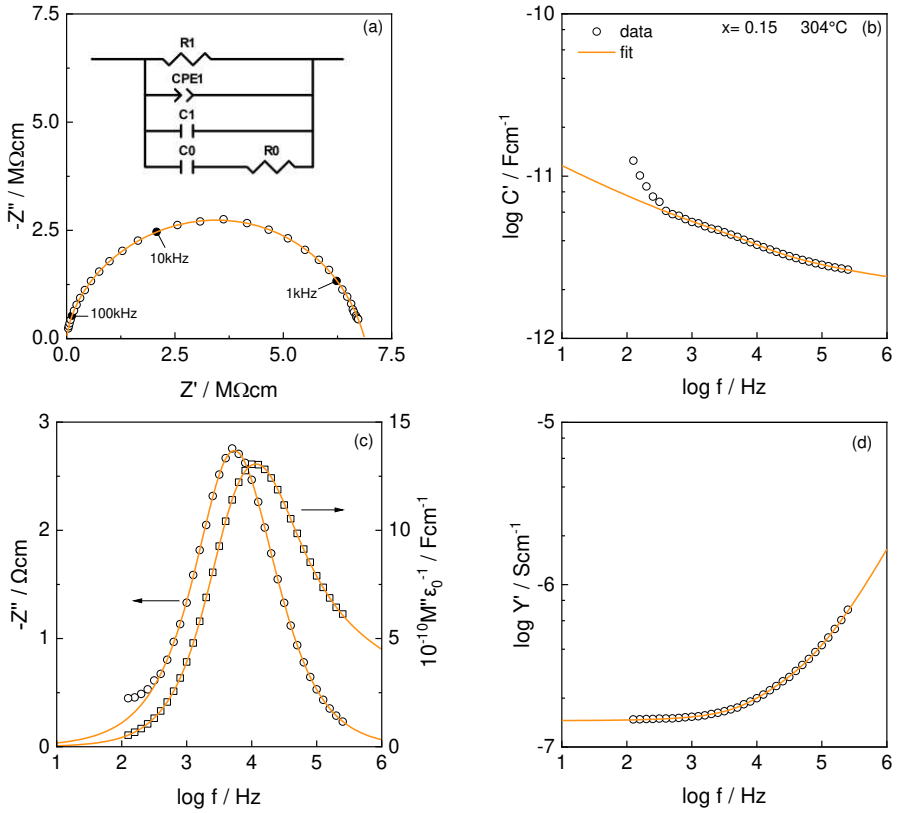

***Figure 7**. Impedance response of x=0.15 at 304°C, fitted to equivalent circuit H.*

We therefore conclude that circuit H is the preferred circuit for two reasons. First, it has the parallel combination of conducting and dielectric elements, which intuitively, seems to be the most logical circuit. Second, together with closely-related circuit G, it has the smallest fit residuals. Circuit C also has low fit residuals, but we exclude this since it would represent a series combination of two impedance components and imply that the sample was electrically inhomogeneous. This circuit was excluded from consideration of fits to single crystal YSZ [14].

Conductivity data for σ_1 (ie R_1^{-1}) have already been given in Fig 3(a) and are reproduced in Fig 8(b), together with data for the dielectric component, σ_0 (ie R_0^{-1}). Two observations may be made. First, as

stated previously, σ_1 *(ie* σ_b*)* decreases with increasing x but its activation energy is unchanged. The conductivity of a material with hopping charge carriers is given by:

$$\sigma = n\, e\, \mu \qquad (1)$$

where *n, e* and μ are the number, charge and mobility of the carriers. Since the activation energy is unchanged with composition, it is likely that the conductivity activation energy is the same as that for migration, or mobility. Therefore, n is temperature-independent for a particular data set but decreases with increasing x; the conductivity reduction is attributed to a reduction in number of mobile oxygen vacancies.

Second, the activation energies for σ_0 and σ_1 are the same for x = 0.12 but that for σ_0 increases with x. This means that, with increasing x, the processes responsible for σ_0 are increasingly different from those responsible for *dc* conduction, σ_1. In particular, the oxygen vacancy hops responsible for the dielectric component or dipole reorientation become more difficult with increasing x.

Fitted data for the dipole or dielectric capacitance, C_0 are shown in Fig 8(a). Two effects are seen:
(i)C_0 values decrease with increasing x. This is consistent with the decrease in σ_0 shown in (b): the dipoles show smaller polarizability or capacitance at the same time as their ease of reorientation, given by σ_0, decreases with x
(ii)C_0 values increase with increasing temperature, (a) and at the same time, σ_0 increases, (b). Again, there is a correlation between increased local conductivity and increased polarizability of the local environment around the hopping oxide ions.

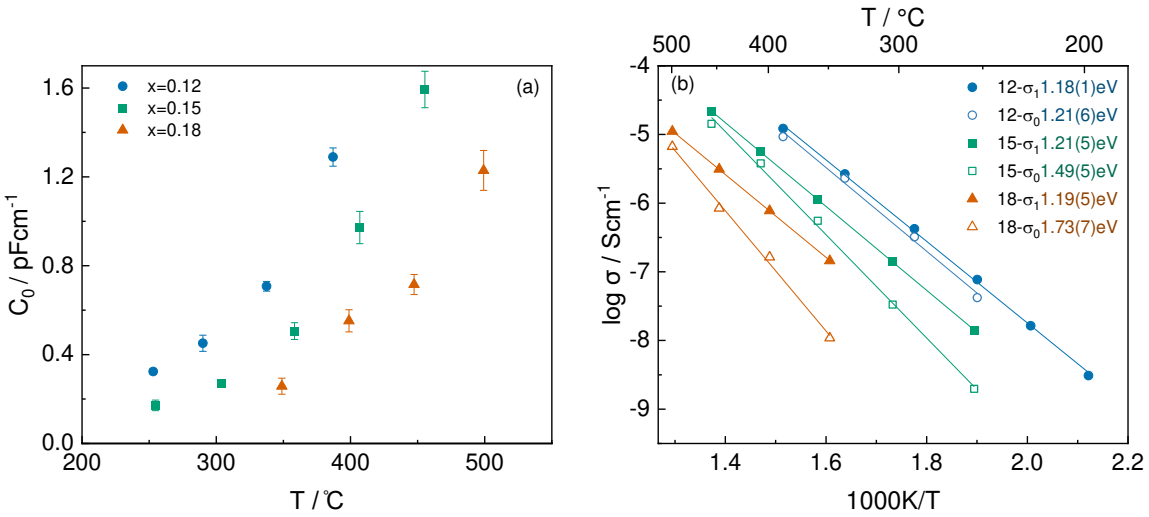

Figure 8. Temperature and composition dependence of dipolar relaxation parameters (a) C_0 and (b) σ_0 ($\equiv R_0^{-1}$) for x=0.12,0.15 and 0.18. Data for σ_1 are included in (b) for comparison.

3.3.2 Grain boundary impedance

The next step in circuit analysis was to consider the grain boundary data. It was found that addition of the parallel element R_2CPE_2 to circuit H gave good fits, as shown for x = 0.15 at 455 °C in Fig 9 and for other compositions and temperatures in Figs S7 and S8. The presence of CPE_2 was required to obtain a good fit, but it was not found necessary to add an additional parallel capacitance C_2 to the circuit. Arrhenius plots for the grain boundary conductivity, σ_{gb} (ie σ_2), are given in Fig 3(a). Within errors, the values obtained were the same as those estimated manually from intercepts of the grain boundary arc, such as seen in Fig 2(a), on the Z' axis. From the similarity in activation energies, we conclude that the

grain boundary material is essentially the same as the bulk CSZ, but the concentration of mobile carriers is different, perhaps due to partial segregation of Ca towards / away from the grain boundaries.

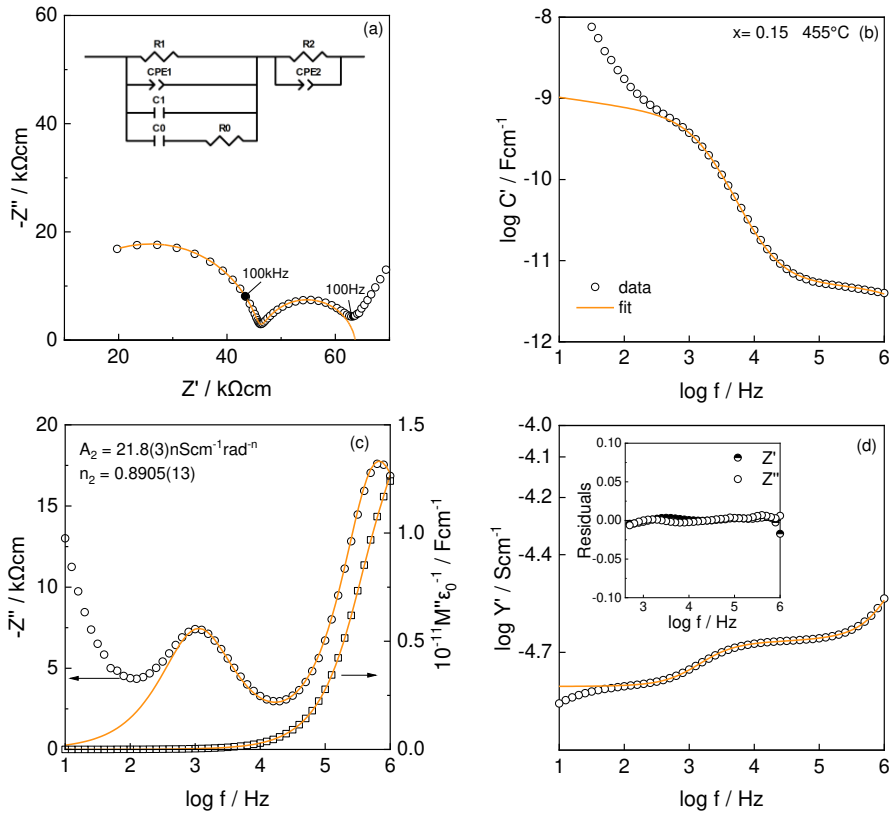

***Figure 9**. Fitting results and residuals of circuit H in series with a parallel R-CPE element that together, represent bulk and grain boundary response of x=0.15 at 455°C.*

3.3.3 Sample-electrode impedance

The final step in circuit analysis was to consider the sample-electrode response. Typical data, Figs 2(a) at 407 °C and 2(e) at 697 °C, show a high impedance effect that dominates the overall response at these temperatures and is characterised by a broad asymmetric arc that appears to have a linear component at the highest frequencies. Various circuits, including the Randles circuit, are considered in the literature and include the possibility of two impedance contributions: (i) a parallel RC element (ideally) in which R represents charge transfer of oxygen species / electrons and is in parallel with a double layer capacitance at the sample-electrode interface; (ii) a Warburg diffusion element that represents oxygen molecules moving towards / away from the interface and involves diffusion through the electrode.

Various circuits that may represent these possibilities were tested for one typical data set and are shown in Fig 10, together with the fit residuals that were obtained. Fitted parameter values are given in Table S4. Due to frequency limitations of the data at high temperatures, the only components of the sample impedance that could be included in the fits were the bulk resistance, R_1 and the grain boundary impedance, R_2CPE_2. The most satisfactory fit for the sample-electrode response is shown in (c) and has components R_3C_3 that appear to represent the charge transfer impedance and R_4CPE_4 that represents the Warburg; this is a finite Warburg which is limited at low frequencies by the parallel resistance, R_4 and

probably, is a characteristic of the electrode material and its microstructure. The fitted impedance response for x=0.15 at 697°C is shown in Fig S9.

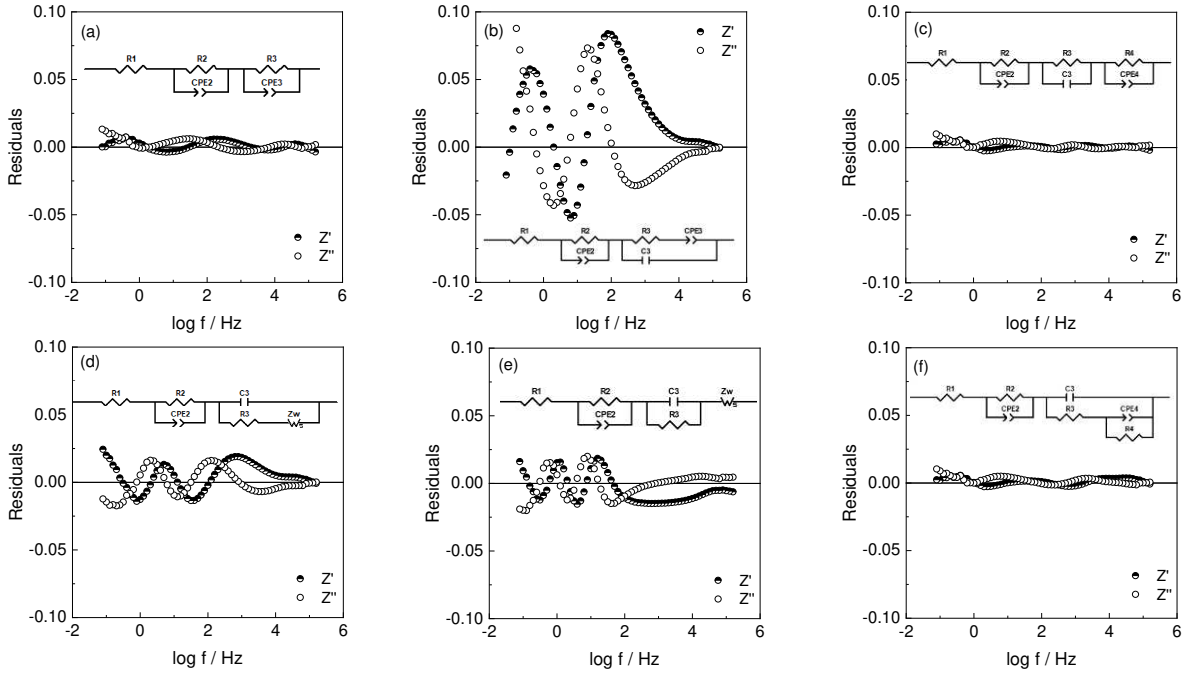

Figure 10. *Fitting residuals from 6 possible equivalent circuits to represent the bulk, grain boundary and electrode response of x=0.15 at 697°C.*

4.Discussion

4.1 Conduction mechanism in CSZ grains and grain boundaries

The decrease in bulk conductivity with increasing x, reported here for compositions in the range 0.12 to 0.18, is consistent with literature reports that show a maximum conductivity around x=0.12 to 0.13 [10], [18], which is just inside the compositional range of the cubic stabilised solid solutions. Comparison of activation energy values with those in the early literature is not straightforward, however, due to (i) the possible contribution of grain boundary impedances to total conductivity data in the early literature, (ii) the effect of curvature in Arrhenius plots at high temperatures and (iii) the possibility of order-disorder phenomena associated with differences in sample history and annealing temperature. Nevertheless, since all Arrhenius plots are essentially parallel, the implication is that the conductivity differences are attributable entirely to differences in mobile carrier concentration; a single conduction mechanism is responsible for the temperatures and compositions studied, as well as for both grain and grain boundary regions.

The reduction in bulk conductivity, and therefore, mobile oxygen vacancy concentration, between compositions 12 and 18% CaO, Fig 8(b), is by a factor of about 20-25. At the same time, the total vacancy concentration increases by 50% as a consequence of the charge compensation mechanism. This means that the *effective* mobile carrier concentration in 18% CaO is only about 3% of that in 12% CaO and indeed, it is by no means certain that all vacancies in 12% CaO are mobile. CSZ may, therefore, be regarded as a *weak electrolyte* [42], [43] in which only a small number of the potential current carriers are dissociated, or mobile. ~~Since the activation energy for bulk conductivity is independent of composition, it seems likely that this is determined by a single parameter, mobility.~~ The conclusion that mobile carrier concentration is independent of temperature in the lower temperature region of linear Arrhenius behaviour agrees with similar conclusions in [44], but disagrees with the conclusion in [44] that all oxygen vacancies are mobile.

The bulk and grain boundary conductivities in the linear, low temperature region have activation energy, 1.15(6) eV, independent of x over the range 0.12 to 0.18. Grain boundary conductivities are apparently ½ to 1 order of magnitude higher than the bulk conductivities, Fig 3(a), but are not corrected for the geometry of the grain boundary regions. Capacitance data, Fig 2(c), show plateaux around 0.1-1 nF that are two orders of magnitude larger than the bulk plateaux. Making the assumption that grain boundary thickness is inversely proportional to grain boundary capacitance [45], the grain boundary resistivities may be up to one order of magnitude larger than grain resistivities. This may reflect a reduction in mobile carrier concentration in the grain boundary regions, possibly due to partial segregation of Ca, and oxygen vacancies away from the grain boundaries. However, similarity of grain and grain boundary activation energies indicates a similarity in structure of the two regions and therefore, that the grain boundary has the character of a constriction resistance, associated probably with incomplete densification of the ceramics [46].

There has been much interest in the literature in the mechanism of conduction by oxygen vacancies in CSZ and in other fluorite-structured materials, especially YSZ. Dopants such as Ca and Y carry different charge to neutral Zr and the oxygen vacancies are also charged, leading to strong electrostatic interactions between dopants and the current carrying species. An early defect structure model was developed [10] that predicted a change in the composition dependence of the conductivity of CSZ which passed through a maximum at a similar composition, x=0.125, to that seen experimentally by several authors. The model was subsequently applied to YSZ compositions [11] to account for experimental data. Nakamura and Wagner [10], [11], suggested that oxide ion conductivity takes place through the dopant-$V_O^{\bullet\bullet}$ path but involves more than one level of dopant-defect association, taking into consideration that every cation has 8-first and 24-second nearest anion neighbour sites. The essence of the model is that vacancy conduction is facilitated best when each substitutional Ca has one of its eight nearest neighbour oxygen sites vacant, in what was described as a 'one-fold dopant-defect associate' or complex involving interactions such as Ca_{Zr}''-$V_O^{\bullet\bullet}$ in CSZ or Y_{Zr}'-$V_O^{\bullet\bullet}$ in YSZ. At composition x = 0.125, these complexes overlap to cover the entire structure which means that long range oxygen vacancy hopping could occur inside the complexes and therefore, the complexes would act to facilitate rather than hinder conduction.

In the Nakamura / Wagner model, migration of un-associated oxygen vacancies requires extra energy compared with that for migration within the complexes and is regarded as the reason for reduced conductivity at smaller x values where the complexes do not link to form a continuous network. At higher x values, more than one oxygen vacancy / Ca is associated with each complex leading to trimers such as Ca_{Zr}''- $V_O^{\bullet\bullet}$ - Ca_{Zr}''. These were thought to bind the oxygen vacancies more strongly, thereby reducing the carrier concentration but also, blocking partially the vacancy migration pathway. Consequently, the conductivity decreases at higher x values. This viewpoint is, however, significantly different from that of many subsequent authors who treated the complexes as instead, traps that require an additional enthalpy of dissociation to liberate 'free' oxygen vacancies.

Various models for defect formation, interaction and association in YSZ and ScSZ have been evaluated in a definitive series of papers by Hull *et al* [27]–[29]. They used a combination of conductivity measurements, diffraction studies, including diffuse scattering, quasielastic scattering and molecular dynamics simulations and were able to investigate the significance of various defect combinations. To summarise briefly the main conclusions:

1.Oxygen vacancies are associated preferentially with Zr rather than with Y, Sc;

2.Cation–oxygen vacancy interactions are mainly responsible for differences in conductivity with different dopants;

3.Oxygen vacancy–oxygen vacancy pairs in the <111> orientation are important in determining the composition–dependence of conductivity for a given dopant;

4.The decrease in conductivity that is generally observed at higher dopant concentrations is attributed to immobilisation of the oxygen vacancy pairs into aggregates with a <112> orientation. Interestingly, these aggregates resemble the oxygen vacancy order in $Zr_3Y_4O_{12}$ and raise the possibility of premonitory segregation of ordered regions within an otherwise-homogeneous solid solution.

The defect structure in CSZ [33] appears to be different from that in YSZ and ScSZ and is limited to single oxygen vacancies and vacancy pairs [27], [31], [32], without evidence for either larger defect aggregates or tetragonal distortions. In all three cases, however, it appears that defect clusters are responsible for reduced conductivity at high x, but is less clear whether single oxygen vacancies or vacancy pairs are responsible for the high conductivity at low x. The role of the acceptor dopant appears not to be dominant in optimising conductivity at low x since the conductivity in all systems decreases with dopant concentration at higher x. For ScSZ, the composition with maximum conductivity varies with measurement temperature and so, in this system at least, there is not a specific composition at which the conductivity is maximised [29].

4.2 Curvature of Arrhenius plots

Early models of the widely-observed curvature in conductivity Arrhenius plots at high temperatures [7]–[13] assumed that dissociation of trapped vacancies was responsible, which would reduce even further the mobile vacancy concentration at lower temperatures. This model may be correct in principle, but alternatively, the carriers may be trapped as oxygen vacancy pairs or larger aggregates that may, or may not, involve cations. There may also be oxygen vacancy pairs that have different separation in <111>, <110> and <100> orientations. Evidence from MD simulations on YSZ and ScSZ indicates that the numbers of pairs of these three types is temperature-dependent [28].

4.3 Dielectric contribution to the bulk impedance

As far as we are aware, no direct experimental evidence for the possible effect of dipoles on electrical properties has been presented previously. Some authors report dielectric measurements with data presented in tan δ format [9], [47]; however, tan δ peaks are not necessarily evidence of dipole re-orientation but can arise simply from series R-C connections that form part of a larger equivalent circuit. The features of our experimental results that need explanation are:

1.At the lowest x value studied, x=0.12, the activation energies for dielectric relaxation or dipole reorientation and bulk conductivity are similar, 1.21 eV, Fig 8(b).
2.With increasing x, the activation energy for the dielectric component is increasingly greater than that for bulk conduction, eg 1.73(7) eV compared with 1.19(5) eV for x=0.18.
3.The dipole capacitance, C_o, increases with temperature but decreases with x, Fig 8(a).

In order to detect dipolar processes in impedance data, it is essential that the processes are (i) localised, (ii) constrained by a series capacitance, C_o and (iii) do not contribute to long range conduction. The logical origin of dipoles would be the association of oppositely-charged oxygen vacancies and calcium dopants, ie $V_o^{\bullet\bullet}$-Ca_{Zr}'', although it is clear that strain effects associated with size mismatch can act to moderate the strength of electrostatic interactions [29]. The results of diffuse scattering measurements on single crystals of CSZ with different composition [31], [32] were interpreted in terms of two types of defect, single oxygen vacancies with relaxed neighbouring ions and oxygen vacancy pairs. Our results showing the composition independence of the bulk activation energy and the decrease in conductivity with x, taken together, indicate that the species responsible for bulk conduction are likely to be isolated oxygen vacancies whose number decreases with increasing x at the same time as the number of oxygen vacancy pairs increases.

The dipoles may correspond to oxygen vacancies that form pairs to either side of a Ca^{2+} ion, oriented in the <111> directions. Dipole reorientation may involve vacancies that hop in either <100> or <110> directions although in both cases, this results in an increase in separation of the Ca_{Zr} and V_O species that form the dipoles. The activation energy for dipole reorientation, σ_0, increases with x, either because their reorientation becomes more difficult with an increase in number of pairs, or because the pairs begin to coalesce into larger aggregates. With increasing temperature, the increase in permittivity, ε', is attributed to increased thermal motion of the dipole components, but with increasing x, ε' decreases due to the increase in dipole cluster strength.

For a structure such as CSZ that contains both short range dielectric and long range conductivity components, there appears to be no *a priori* reason why the local process should have either higher or lower activation energy than long range conduction. From our results on CSZ, the short range conduction has either similar (x=0.12) or greater (x=0.15, 0.18) activation energy, whereas for YSZ single crystal [14], its value was less. The similarity in activation energy for x=0.12 could indicate that the first hop is the same for both long range conduction and short range dielectric processes, but the distinction arises over the possibility of second, and subsequent hops; clearly in the dielectric case, follow-on hops are blocked.

5. Conclusions

The bulk conductivity of CSZ ceramics decreases with increasing x but the activation energy is unchanged. This means that the activation energy is controlled by the activation energy for migration, or hopping, of oxygen vacancies.

The magnitude of the conductivity is controlled by the number of *mobile* oxygen vacancies which decreases greatly with x. The number of oxygen vacancies that are mobile is small, ≤3% at high x, indicating that CSZ may be regarded as a weak electrolyte. The number of mobile vacancies is temperature-independent for 12, 15 and 18% CaO, at least in the lower temperature region of linear Arrhenius behaviour.

The mechanism responsible for increased immobilisation of the oxygen vacancies with increasing x is tentatively attributed to the formation of oxygen vacancy pairs and/or larger aggregates, similar to those that have been identified in YSZ and ScSZ.

The impedance data show the presence of a local dielectric loss or conductivity in addition to long range conduction. The logical explanation for this is that local hops occur but without the possibility of follow-on hops. It is difficult to see how oxygen vacancy pairs alone could lead to dipoles. These are therefore attributed to $Ca_{Zr} - V_o$ pairs or larger defect groupings.

Although oxygen vacancy pairs and defect dipoles are both in evidence, the precise factors that control the ionic conductivity, its activation energy and high temperature curvature in Arrhenius plots are still not fully resolved. The species that are responsible for long range conduction appear to involve a minority of the potentially mobile oxygen vacancies, which complicates their study by most characterisation techniques.

The presence of local conduction processes such as dipole reorientation, in parallel with long range conduction, does not affect the value of the sample bulk conductivity but is apparent on fitting impedance data to the most appropriate equivalent circuit.

Acknowledgements

JRG thanks CONACyT for a studentship, grant number 578893 and the CDT in Energy Storage and its Applications for assistance with conference expenses.

[1] B. C. H. Steele, “Oxygen ion conductors and their technological applications,” *Mater. Sci. Eng. B*, vol. 13, no. 2, pp. 79–87, 1992.

[2] A. B. Stambouli and E. Traversa, “Solid oxide fuel cells (SOFCs): a review of an environmentally clean and efficient source of energy,” *Renew. Sustain. Energy Rev.*, vol. 6, pp. 433–455, 2002.

[3] S. A. Sternbergh and W. M. Hickam, “Flight type oxygen partial pressure sensor,” Pittsburgh, Pa., 1966.

[4] J. W. Fergus, “Doping and defect association in oxides for use in oxygen sensors,” *J. Mater.*

Sci., vol. 38, no. 21, pp. 4259–4270, 2003.

[5] S. J. Skinner and J. A. Kilner, "Oxygen ion conductors," *Mater. Today*, vol. 6, no. 3, pp. 30–37, 2003.

[6] M. C. Steil, F. Thevenot, and M. Kleitz, "Densification of Yttria - Stabilized Zirconia Impedance Spectroscopy Analysis," *J. Electrochem. Soc.*, vol. 144, no. 1, pp. 390–398, 1997.

[7] T. Y. Tien and E. C. Subbarao, "X-Ray and Electrical Conductivity Study of the Fluorite Phase in the System ZrO2 –CaO," *J. Chem. Phys.*, vol. 39, pp. 1041–1047, 1963.

[8] M. Asadikiya and Y. Zhong, "Oxygen ion mobility and conductivity prediction in cubic yttria-stabilized zirconia single crystals," *J. Mater. Sci.*, vol. 53, no. 3, pp. 1699–1709, 2018.

[9] S. Komine and F. Munakata, "Dielectric relaxation analysis for 8 mol% YSZ single crystal," *J. Mater. Sci.*, vol. 40, no. 15, pp. 3887–3890, 2005.

[10] A. Nakamura and J. B. Wagner, "Defect Structure, Ionic Conductivity, and Diffusion in Calcia-Stabilized Zirconia," *J. Electrochem. Soc.*, vol. 127, no. 11, pp. 2325–2333, 1980.

[11] A. Nakamura and J. B. Wagner, "Defect Structure, Ionic Conductivity, and Diffusion in Yttria Stabilized Zirconia and Related Oxide Electrolytes with Fluorite Structure," *J. Electrochem. Soc.*, vol. 133, no. 8, p. 1542, 1986.

[12] J. A. Kilner and R. J. Brook, "A study of oxygen ion conductivity in doped non-stoichiometric oxides," *Solid State Ionics*, vol. 6, no. 3, pp. 237–252, 1982.

[13] D. K. Honke, "Ionic conduction in doped zirconia," in *Fast Ion Transport in Solids, Electrodes and Electrolytes*, 1979, pp. 669–672.

[14] X. Vendrell and A. R. West, "Electrical Properties of Yttria-Stabilized Zirconia, YSZ Single Crystal: Local AC and Long Range DC Conduction," *J. Electrochem. Soc.*, vol. 165, no. 11, pp. F966–F975, 2018.

[15] N. Masó and A. R. West, "Electronic conductivity in Yttria-stabilized zirconia under a small dc bias," *Chem. Mater.*, vol. 27, no. 5, pp. 1552–1558, 2015.

[16] M. Jovaní, H. Beltrán-Mir, E. Cordoncillo, and A. R. West, "Atmosphere- and Voltage-Dependent Electronic Conductivity of Oxide-Ion-Conducting Zr1-xYxO2-x/2 Ceramics," *Inorg. Chem.*, vol. 56, no. 12, pp. 7081–7088, 2017.

[17] M. Cologna, B. Rashkova, and R. Raj, "Flash sintering of nanograin zirconia in < 5s at 850°C," *J. Am. Ceram. Soc.*, vol. 93, no. 11, pp. 3556–3559, 2010.

[18] T. H. Etsell and S. N. Flengas, "The electrical properties of solid oxide electrolytes," *Chem. Rev.*, vol. 70, no. 3, pp. 339–376, 1970.

[19] R. Terki, G. Bertrand, H. Aourag, and C. Coddet, "Structural and electronic properties of zirconia phases: A FP-LAPW investigations," *Mater. Sci. Semicond. Process.*, vol. 9, no. 6, pp. 1006–1013, 2006.

[20] S. Y. Kwon and I. H. Jung, "Critical evaluation and thermodynamic optimization of the CaO-ZrO2 and SiO2-ZrO2 systems," *J. Eur. Ceram. Soc.*, vol. 37, no. 3, pp. 1105–1116, 2017.

[21] K. Kiukkola and C. Wagner, "Measurements on Galvanic Cells Involving Solid Electrolytes," *J. Electrochem. Soc.*, vol. 104, no. 6, pp. 379–387, 1957.

[22] A. M. Diness and R. Roy, "Experimental confirmation of major change of defect type with temperature and composition in ionic solids," *Solid State Commun.*, vol. 3, no. 6, pp. 123–125, 1965.

[23] T. H. Etsell and S. N. Flengas, "N - type Conductivity in Stabilized Zirconia Solid

Electrolytes," *J. Electrochem. Soc.*, vol. 119, no. 1, pp. 1–7, 1972.

[24] F. A. Kröger, "Electronic Conductivity of Calcia-Stabilized Zirconia," *J. Am. Ceram. Soc.*, vol. 49, no. 4, pp. 215–218, 1966.

[25] J. Rudolph, "Mechanism of conduction in oxide semiconductors at high temperatures," *Zeitschrift für Naturforsch.*, vol. 14, no. 8, pp. 727–737, 1959.

[26] R. W. Vest, N. M. Tallan, and W. C. Tripp, "Electrical Properties and Defect Structure of Zirconia: I, Monoclinic Phase," *J. Am. Ceram. Soc.*, vol. 47, no. 12, pp. 635–640, Dec. 1964.

[27] J. P. Goff, W. Hayes, S. Hull, M. T. Hutchings, and K. N. Clausen, "Defect structure of yttria-stabilized zirconia and its influence on the ionic conductivity at elevated temperatures," *Phys. Rev. B - Condens. Matter Mater. Phys.*, vol. 59, no. 22, pp. 14202–14219, 1999.

[28] S. T. Norberg *et al.*, " Structural Disorder in Doped Zirconias, Part I: The Zr 0.8 Sc 0.2− x Y x O 1.9 ($0.0 \leq x \leq 0.2$) System ," *Chem. Mater.*, vol. 23, no. 6, pp. 1356–1364, 2011.

[29] D. Marrocchelli, P. A. Madden, S. T. Norberg, and S. Hull, "Structural Disorder in Doped Zirconias, Part II: Vacancy Ordering Effects and the Conductivity Maximum.," *Chem. Mater.*, vol. 23, no. 6, pp. 1365–1373, 2011.

[30] A. Bogicevic and C. Wolverton, "Nature and strength of defect interactions in cubic stabilized zirconia," *Phys. Rev. B - Condens. Matter Mater. Phys.*, vol. 67, no. 2, 2003.

[31] T. Proffen, R. B. Neder, F. Frey, and W. Assmus, "Defect structure and diffuse scattering of zirconia single crystals doped with 7 mol% CaO," *Acta Crystallogr. Sect. B*, vol. 49, no. 4, pp. 599–604, 1993.

[32] T. Proffen, R. B. Neder, F. Frey, D. A. Keen, and C. M. E. Zeyen, "Defect structure and diffuse scattering of zirconia single crystals with 10 and 15 mol% CaO at temperatures up to 1750 K," *Acta Crystallogr. Sect. B*, vol. 49, no. 4, pp. 605–610, 1993.

[33] S. Jing-ze and W. Yu-ming, "Diffusion in Fast-Ion Conductor Calcia-Stabilized Zirconia: a Molecular Dynamics Study," *Chinese Phys. Lett.*, vol. 15, no. 10, p. 727, 1998.

[34] S. Kazlauskas, A. Kežionis, T. Šalkus, and A. F. Orliukas, "Electrical properties of YSZ and CaSZ single crystals," *Solid State Ionics*, vol. 231, pp. 37–42, 2013.

[35] O. Y. Kurapova, O. V Glumov, M. M. Pivovarov, S. N. Golubev, and V. G. Konakov, "Structure and conductivity of calcia stabilized zirconia ceramics, manufactured from freeze-dried nanopowder," *Rev. Adv. Mater. Sci.*, vol. 52, no. 1–2, pp. 134–141, 2017.

[36] C. Schwandt and W. Weppner, "Electrode reactions at oxygen, noble metal / stabilized zirconia interfaces," *Ionics (Kiel).*, vol. 2, no. 2, pp. 113–122, 1996.

[37] J. E. B. Randles, "Kinetics of rapid electrode reactions," *Faraday Discuss.*, vol. 1, pp. 11–19, 1947.

[38] S. Pandey, D. Kumar, O. Parkash, and L. Pandey, "Equivalent circuit models using CPE for impedance spectroscopy of electronic ceramics," *Integr. Ferroelectr.*, vol. 183, no. 1, pp. 141–162, 2017.

[39] N. H. Perry, T. C. Yeh, and T. O. Mason, "Temperature dependence of effective grain core/single crystal dielectric constants for acceptor-doped oxygen ion conductors," *J. Am. Ceram. Soc.*, vol. 94, no. 2, pp. 508–515, 2011.

[40] A. Software and O. Manual, "ZView." 2016.

[41] M. A. Hernandez and A. R. West, "Dipolar relaxation and impedance of an yttria-stabilised zirconia ceramic electrolyte," *J. Mater. Chem. A*, vol. 4, no. 4, pp. 1298–1305, 2016.

[42] M. D. Ingram, C. T. Moynihan, and A. V. Lesikar, “Ionic conductivity and the weak electrolyte theory of glass,” *J. Non. Cryst. Solids*, vol. 38–39, no. PART 1, pp. 371–376, 1980.

[43] J. L. Souquet and W. G. Perera, “Thermodynamics applied to ionic transport in glasses,” *Solid State Ionics*, 1990.

[44] A. Orliukas, P. Bohac, K. Sasaki, and L. Gauckler, “Relaxation dispersion of ionic conductivity in a Zr0.85Ca0.15O1.85 single crystal,” *J. Eur. Ceram. Soc.*, vol. 12, no. 2, pp. 87–96, 1993.

[45] J. T. S. Irvine, D. C. Sinclair, and A. R. West, “Electroceramics: Characterization by Impedance Spectroscopy,” *Adv. Mater.*, vol. 2, no. 3, pp. 132–138, 1990.

[46] Y. Li, M. Liu, J. Gong, Y. Chen, Z. Tang, and Z. Zhang, “Grain-boundary effect in zirconia stabilized with yttria and calcia by electrical measurements,” *Mater. Sci. Eng. B Solid-State Mater. Adv. Technol.*, vol. 103, no. 2, pp. 108–114, 2003.

[47] H. Yamamura, Y. Yagi, and K. Kakinuma, “Dielectric relaxations of Y-Doped ZrO2 single crystal,” *J. Ceram. Soc. Japan*, vol. 115, no. 1345, pp. 546–550, 2007.

Supplementary

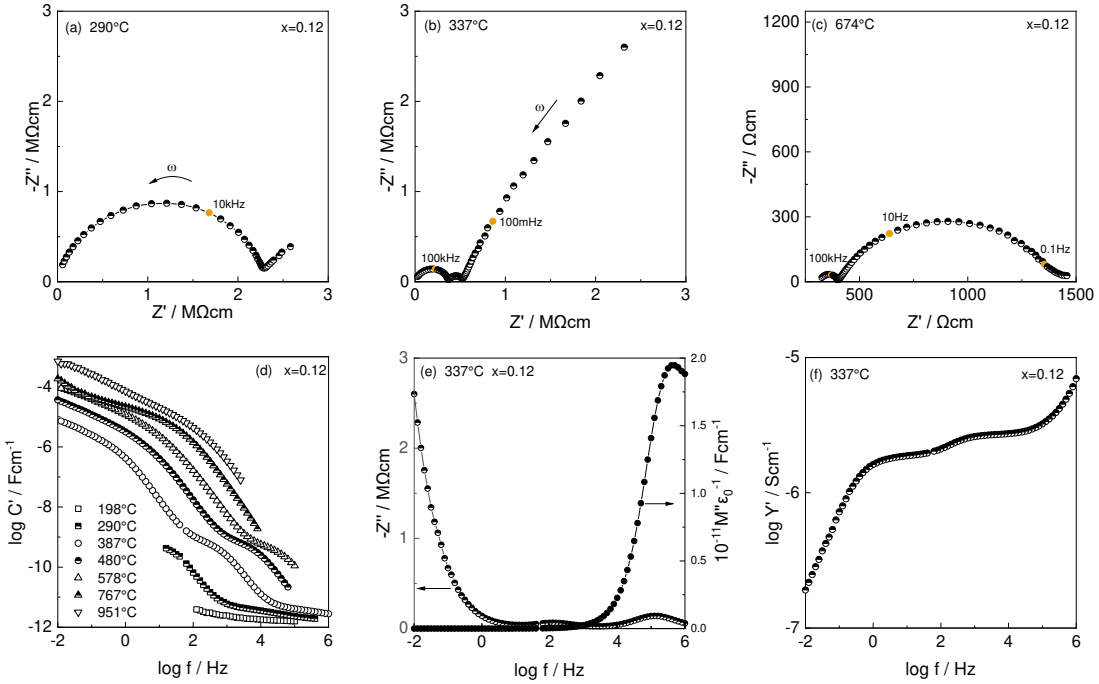

***Figure S1**. (a)-(c) Impedance complex plane plots and spectroscopic plots of (d) capacitance, (e) Z''/M'' and (f) admittance at different temperatures for x=0.12; ω =2πf.*

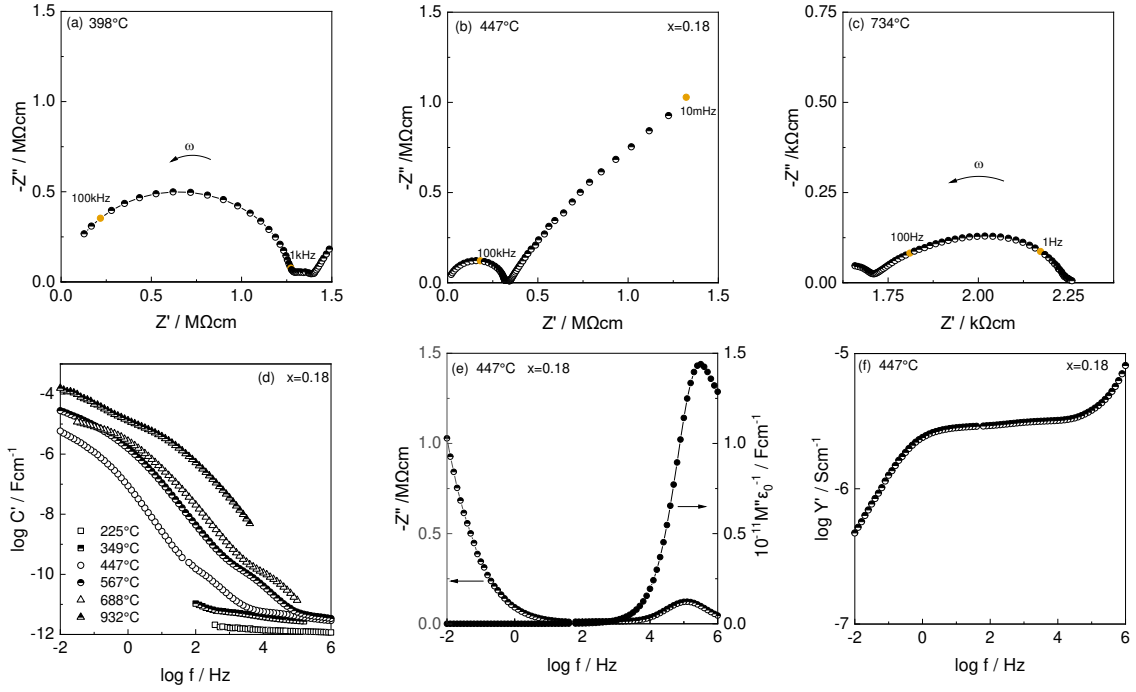

***Figure S2**. (a)-(c) Impedance complex plane plots and spectroscopic plots of (d) capacitance, (e) Z''/M'' and (f) admittance spectroscopic plots at different temperatures for x=0.18; ω =2πf.*

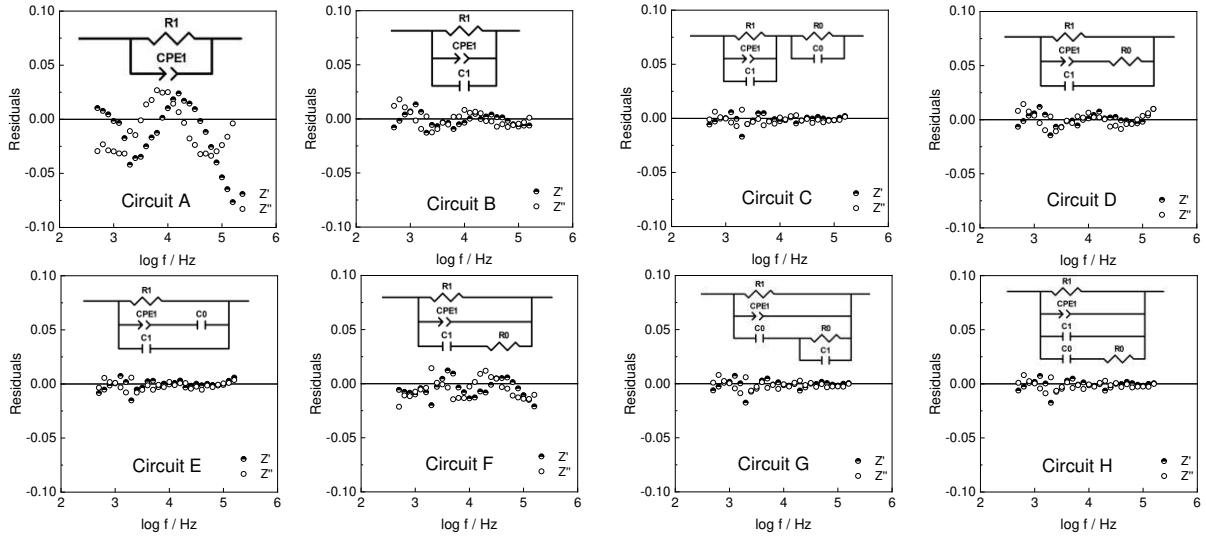

***Figure S3**. Fitting residuals of the bulk response from 8 possible equivalent circuits for x=0.12 at 253°C.*

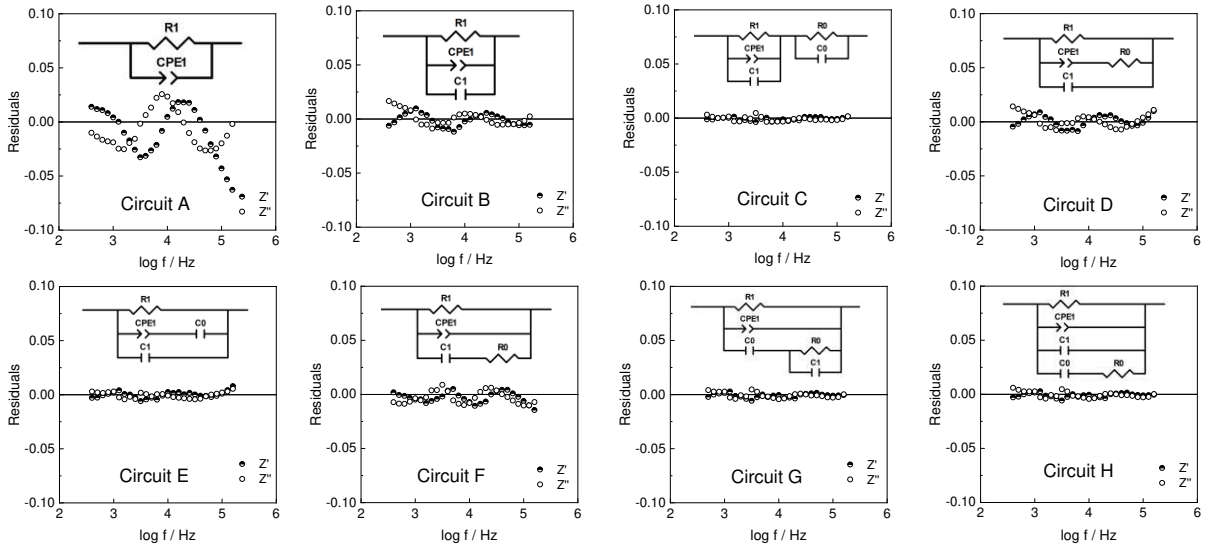

***Figure S4**. Fitting residuals of the bulk response from 8 possible equivalent circuits for x=0.18 at 349°C.*

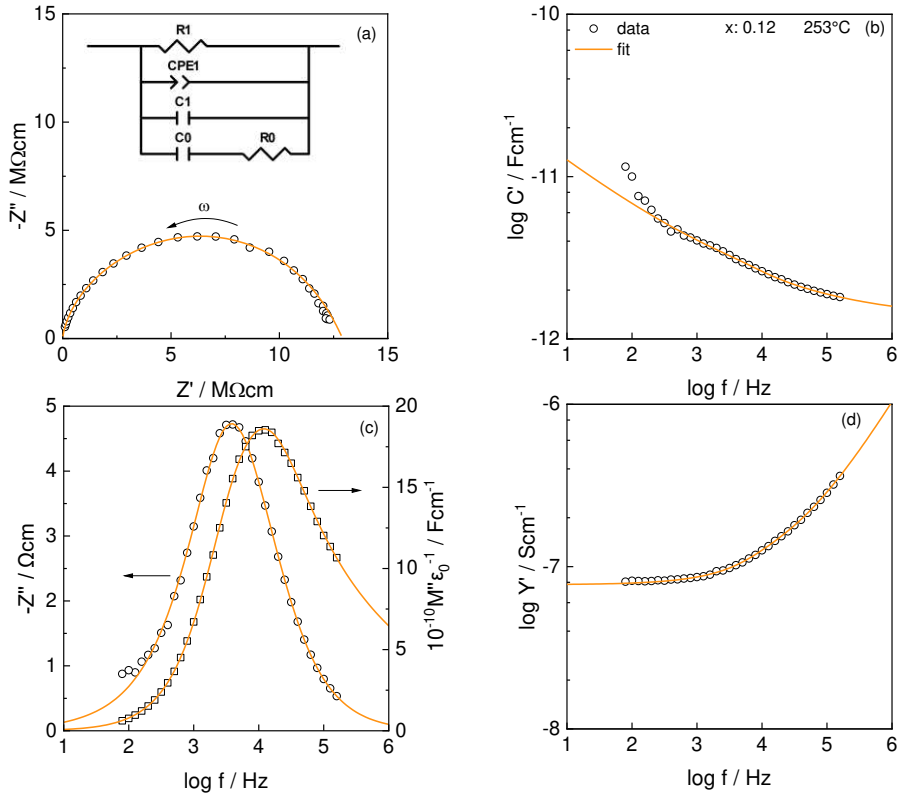

***Figure S5**. Impedance response of x=0.12 at 253°C, fitted to equivalent circuit H.*

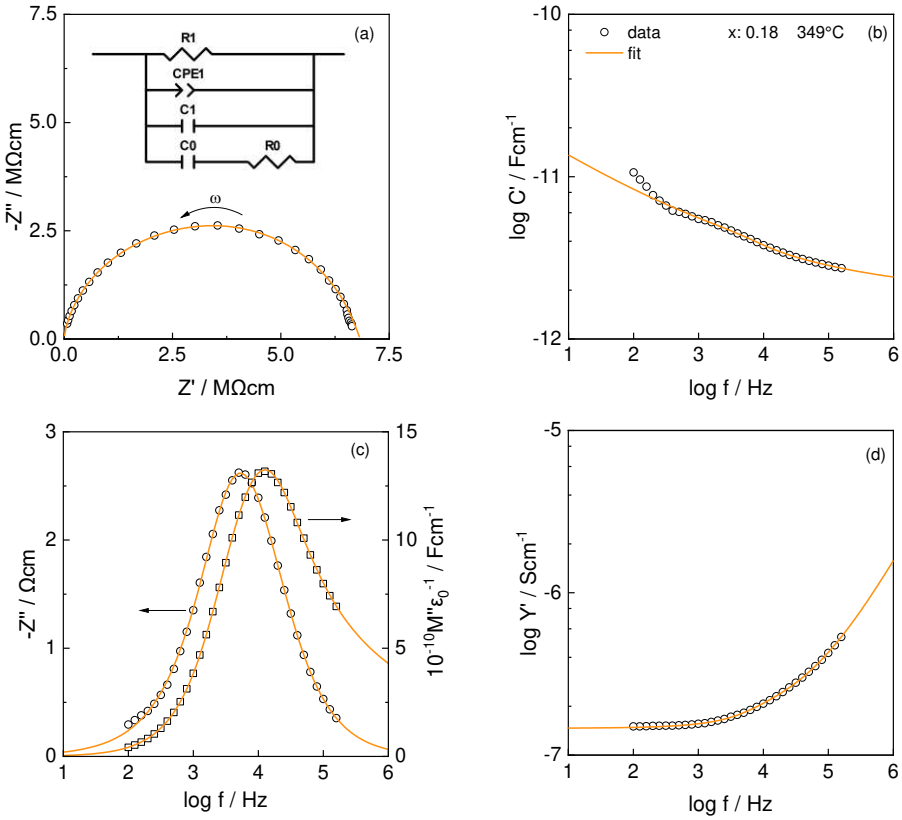

***Figure S6**. Impedance response of x=0.18 at 349°C, fitted to equivalent circuit H.*

***Table S1**. Fitted parameters of the different circuits tested for the bulk response, x=0.15 at 304°C.*

Circuit	R_1 (MΩcm)	R_0 (MΩcm)	A_1 ($pScm^{-1}rad^{-n}$)	n_1	C_1 ($pFcm^{-1}$)	C_0 ($pFcm^{-1}$)	X^2 ($x10^{-5}$)	Weighted Sum of Squares ($x10^{-3}$)
A	6.7(5)	–	13.7(5)	0.884(3)	–	–	128	65
B	7.02(2)	–	48(3)	0.715(7)	1.89(3)	–	11	5.5
C	5.3(8)	1.6(8)	73(6)	0.688(7)	2.16(3)	2.7(2)	1.6	0.8
D	7.03(5)	0.8(1)	59(4)	0.677(6)	2.41(2)	–	12	6.3
E	6.8(2)	–	29(4)	0.56(1)	2.18(2)	5.7(4)	3.6	1.8
F	6.7(2)	26(2)	9.1(2)	0.913(2)	7.8(4)	–	14	6.9
G	6.8(1)	1.0(1)	28(1)	0.759(5)	12.2(9)	2.12(2)	1.4	0.7
H	6.8(1)	47(3)	28(1)	0.759(5)	1.81(3)	0.31(2)	1.4	0.7

***Table S2**. Fitted parameters of the different circuits tested for the bulk response, x=0.12 at 253°C.*

Circuit	R_1 (MΩcm)	R_0 (MΩcm)	A_1 ($pScm^{-1}rad^{-n}$)	n_1	C_1 ($pFcm^{-1}$)	C_0 ($pFcm^{-1}$)	X^2 ($x10^{-5}$)	Weighted Sum of Squares ($x10^{-3}$)
A	12.1(2)	–	13.5(7)	0.854(4)	–	–	222.4	108.9
B	13.3(7)	–	71(5)	0.650(7)	1.32(2)	–	14.4	6.909
C	10.7(3)	2.3(2)	103(14)	0.62(1)	1.46(3)	27(3)	5.4	2.471
D	13.1(7)	1.7(2)	67.(5)	0.645(7)	1.64(2)	–	11.6	5.455
E	12.5(5)	–	323(43)	0.52(1)	1.48(1)	5.3(4)	5.7	2.671
F	12.3(6)	40(3)	7.7(3)	0.895(3)	0.84(5)	–	32.7	15.387
G	12.9(6)	1.8(4)	48(5)	0.58(1)	9(1)	1.54(3)	6.0	2.776
H	12.9(6)	23(3)	107(5)	0.58(1)	1.56(2)	0.32(1)	6.0	2.776

***Table S3**. Fitted parameters of the different circuits tested for the bulk response, x=0.18 at 349°C.*

Circuit	R_1 (MΩcm)	R_0 (MΩcm)	A_1 ($pScm^{-1}rad^{-n}$)	n_1	C_1 ($pFcm^{-1}$)	C_0 ($pFcm^{-1}$)	X^2 ($x10^{-5}$)	Weighted Sum of Squares ($x10^{-3}$)
A	6.6(5)	–	15.9(7)	0.872(4)	–	–	164.9	84.079
B	6.9(2)	–	63(2)	0.692(3)	1.91(3)	–	10.6	5.538
C	5.3(7)	1.4(6)	74(6)	0.679(7)	2.16(3)	38(2)	1.4	0.676
D	6.9(3)	1.3(2)	75(7)	0.660(8)	2.50(2)	–	12.2	6
E	6.7(1)	–	497(53)	0.514(9)	2.29(2)	6.0(3)	2.9	1.444
F	6.6(2)	2.8(2)	9.7(3)	0.908(2)	1.05(4)	–	14.2	6.941
G	6.8(2)	1.8(2)	38(3)	0.728(9)	10.3(9)	2.34(3)	1.9	0.918
H	6.8(2)	52(4)	38(3)	0.728(9)	1.91(3)	0.43(4)	1.9	0.918

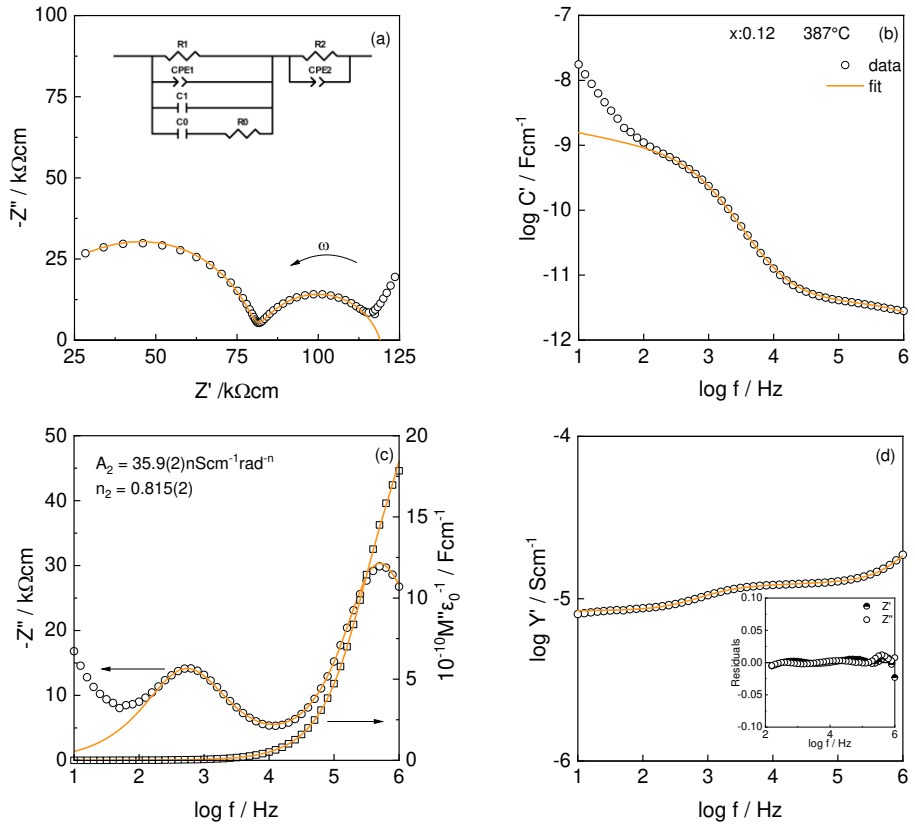

***Figure S7**. Fitting results and residuals of circuit H in series with a parallel R-CPE element that together, represent bulk and grain boundary response of x=0.12 at 387°C.*

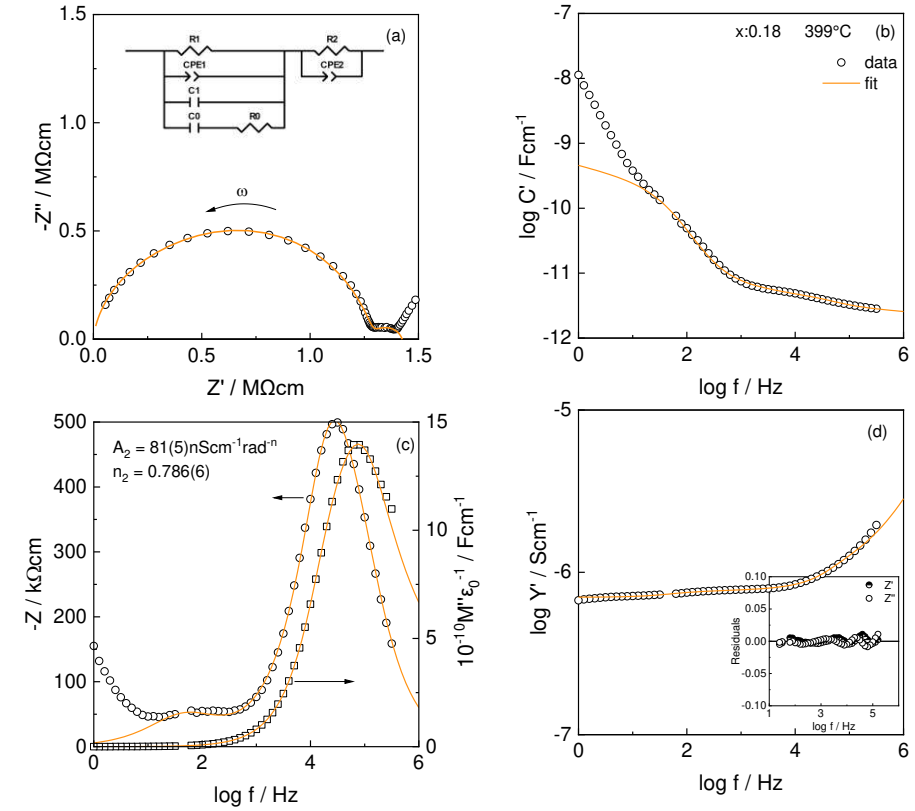

***Figure S8**. Fitting results and residuals of circuit H in series with a parallel R-CPE element that together, represent bulk and grain boundary response of x=0.18 at 399°C.*

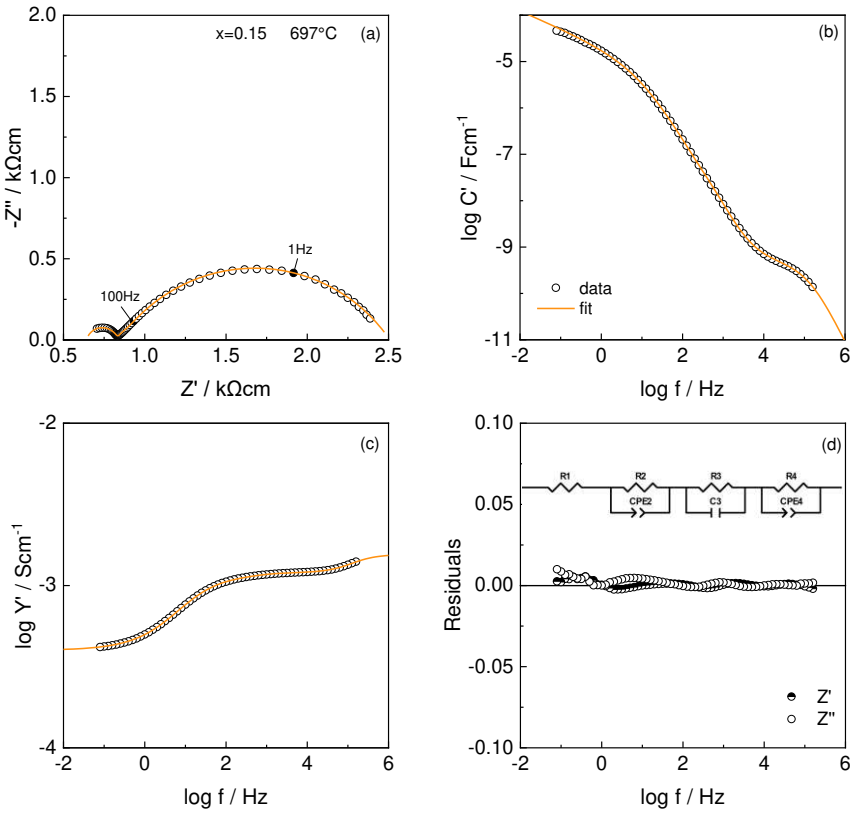

***Figure S9**. Impedance response of x=0.15 at 697°C, fitted to equivalent in Figure 10(c).*

***Table S4**. Fitted parameters of the different circuits tested for the electrode response, x=0.15 at 697°C.*

Circuit	R_3 (Ωcm)	$R_{4/ZWs}$ (Ωcm)	A_3 ($mScm^{-1}rad^{-n}$)	n_3	$A_{4/ZWs}$ ($mScm^{-1}rad^{-n}$)	$n_{4/ZWs}$	C_3 (μFcm^{-1})	X^2 ($x10^{-5}$)	Weighted Sum of Squares ($x10^{-3}$)
1.R3CPE3	1705(6)	-	0.125(1)	0.603(2)	-	-	-	15.76	127.7
2.(CPE3-R3)C3	$2.1x10^{-6}$(4)	-	0.67(2)	0.16(1)	-	-	11.8(9)	1963.9	1610.4
3.(R3C3)-(R4CPE4)	15.4(2)	1671(5)	-	-	$121.4x10^{-3}$(9)	0.618(2)	1.26(6)	1.93	1.35
4. (Zw_s-R3)C3	$1.6x10^{-5}$(7)	1552(12)	-	-	274(9)	0.275(9)	3.1(2)	114.85	141.27
5.(R3C3)-Zw_s	626(20)	906(22)	-	-	72(4)	0.072(4)	376(3)	114.68	141.05
6.(R-(CPER4))C3	39(2)	1650(5)	-	-	$142.6x10^{-3}$(8)	0.611(2)	1.60(8)	8.75	10.76